

Synchrotron X-ray Tomography for 3D Chemical Distribution Measurement of a Flame Retardant and Synergist in a Fiberglass-Reinforced Polymer Blend

Heath A. Barnett,[†] Kyungmin Ham,[‡] Jason T. Scorsone,[†] and Leslie G. Butler^{*,†}

Department of Chemistry, Louisiana State University, Baton Rouge, Louisiana 70803, and Center for Advanced Microstructures and Devices, Louisiana State University, Baton Rouge, Louisiana 70806

Received: September 29, 2008; Revised Manuscript Received: August 3, 2009

A fiberglass-reinforced polymer blend with a new-generation flame retardant is studied with multienergy synchrotron X-ray tomography to assess the blend homogeneity. Relative to other composite materials, this sample is difficult to image due to low X-ray contrast between the fiberglass reinforcement and the polymer blend. Also, the glass fibers are only slightly larger than the 3.26 μm voxels and, due to their high concentration, exist as partially aligned bundles in the polymer matrix. To investigate the chemical composition surrounding the glass fibers, new procedures were developed to find and mark the fiberglass and then assess the flame retardant distribution near the fiber bundles. On the basis of the multienergy imaging across Br and Sb K-edges, the absorbance values were converted to volume percent concentrations. Besides the basic question of the successful and stable blending of the flame retardant and synergist within the polymer matrix, we are also interested in precipitation reactions that might concentrate or diminish concentrations in the close vicinity of the fiberglass reinforcement. Thus, a procedure was developed to analyze radial concentrations about selected, well-isolated fiberglass bundles. Overall, the results show a nicely homogeneous system to the level of the tomography resolution, 3.26 μm , with some enhanced concentration near, ~ 20 μm , the fiber bundles.

Introduction

The dream of 3D chemical analysis for materials science investigations is coming true with new advances in data acquisition and image processing.^{1–5} Recently, synchrotron X-ray tomography has developed into a fast, reliable method for three-dimensional imaging of materials at the micrometer distance scale.^{6–11} While invasive microtome-and-image still has applications in geology,¹² biology,¹³ and the Visible Human Project,¹⁴ full 3D imaging methods are needed in materials science for reasons of sample throughput and data quality. In this work, we investigate the 3D concentration distribution of a flame retardant throughout a polymer blend, especially at the interface with fiberglass reinforcement bundles.

Three-dimensional, and even higher dimensionality, imaging is used to investigate a variety of polymer structure and processing issues. For the new process of high shear rate thermoplastic powder injection molding, synchrotron X-ray tomography of silica particles within the matrix shows flow effects beyond those predicted with Newtonian flow models, indicative of wall slip or surface roughness in the mold.¹⁵ A laboratory microfocus X-ray source yielding images with near 4 μm voxel size at 25 keV was used to image voids and cracks in fiber-reinforced composite laminates.¹⁶ To more easily visualize cracks, an X-ray dye was forced into the sample, thus enabling observation of cracks with sizes on the order of 20% of the voxel size. X-ray absorbance tomography can yield inadequate contrast for blends with similar elemental composition; in that case, X-ray refraction differences can sometimes be used to enhance contrast, as shown for a blend of polystyrene and polymethylmethacrylate (PMMA), imaged at 17.7 keV with 3.14 μm voxel size.¹⁷ A high-strength, thermal-insulating foam,

consisting of glass hollow microspheres imbedded in an epoxy resin, was imaged in 3D at 9.7 keV.¹⁸ The microsphere mean diameter was 35 μm , which was resolved nicely with the 0.7 μm voxel size. The images clearly show the three-phase system, glass, air, and resin. The images were then analyzed to yield the microsphere size distributions, both sphere diameter and wall thickness. Interestingly, refraction effects, used to their advantage by Momose et al.,¹⁷ created minor analysis problems for the microsphere detection. X-ray fluorescence tomography was used to study uptake of Pt(II) and Pt(IV) anticancer drugs in growing tissues; concentration data were presented as a radial concentration profile through the near-spherical tumor sample.¹⁹ In a recent work in electron microscopy tomography, multienergy images were used to separate two components of interest, multiwalled carbon nanotubes and a nylon matrix; the authors note the 4D character of the work, with three spatial dimensions and one chemical analysis dimension.²⁰ TEM and electron microscopy tomography of nickel oxide nanoparticles in an ordered mesoporous material showed the unique advantages of 3D imaging.²¹ The pore structure in poly(vinyl chloride) foams has been studied with tomography and a mean intercept technique.²² A laboratory X-ray source was used to image CO₂-foamed samples of polymethylmethacrylate. Eight samples were measured after different exposure times, and the foam thickness growth rate about the solid PMMA core was shown to be a result of non-Fickian CO₂ diffusion.²³ The structures of star-terpolymers containing interpenetrating columns, with diameters on the order of 20 nm, are imaged by reactive metal staining followed by electron microscopy tomography.^{24,25}

Some flame retardants exhibit interesting dissolution or precipitation properties, depending upon blend compatibility. We previously used 3D tomography to assess the dissolution and molecular diffusion of BT-93 into polystyrene, where extremely slow diffusion rates, on the order of 10^{–17} m²/s, can be detected.²⁶ Also, we performed a number of simulated

* To whom correspondence should be addressed. E-mail: lbutler@lsu.edu.

[†] Department of Chemistry.

[‡] Center for Advanced Microstructures and Devices.

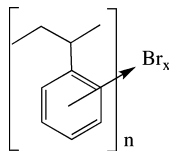


Figure 1. Chemical structure of brominated polystyrene ($x = 3$) used as a flame retardant (FR).

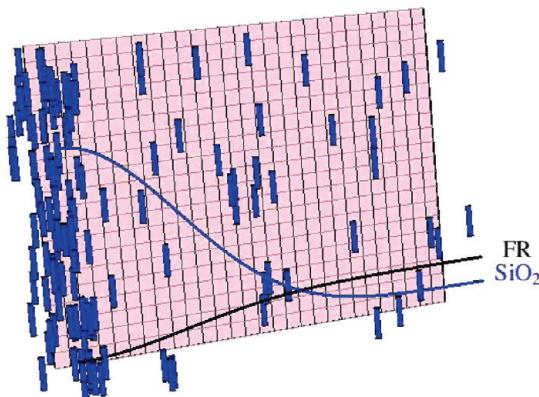


Figure 2. Small glass fibers will assemble into crude bundles in the extruded polymer sample. In tomography, the concentration of FR is measured in cubic volume elements (voxels). The volume elements can be partially occupied by SiO_2 , which should cause the FR concentration to decrease within the bundles.

tomography experiments to explore instrumentation parameters critical to accurate 3D chemical composition mapping with synchrotron X-ray tomography. The experimental parameters included CCD camera specifications, multispectral X-ray imaging, and how these parameters affect the composition maps.²⁷

Fiberglass-reinforced thermoplastics have utility in applications, and selecting the proper blend for a task is important. In some applications, there is the potential for ignition,²⁸ hence the blending with a flame retardant.^{29–31} One high-performance flame retardant is a short-chain, partially brominated polystyrene (FR), (Figure 1), enhanced with a synergist, antimony(III) oxide, Sb_2O_3 . A model for the interaction of fiberglass, a polymer matrix, and the flame retardant is shown in Figure 2. The model is based on the tendency of the fiberglass to form bundles and the question of whether or not the flame retardant concentration responds to those bundles based simply the space-filling effect of fiberglass or a possible thermodynamic enhancement or reduction of the flame retardant concentration in the vicinity of these bundles.

In a previous investigation of a flame retardant/polystyrene blend,¹⁰ we developed some of the techniques used herein, especially the concept of imaging with X-ray energies that span important features in the Br and Sb absorbances. In that work, the flame retardant Saytex BT-93, a brominated aromatic, combined with a synergist, antimony(III) oxide, were found to have a rather heterogeneous distribution in the polystyrene blend. In contrast, in this work, we find the short-chain, partially brominated polystyrene to be much more evenly distributed throughout the polymer matrix. However, the introduction of a fiberglass reinforcement creates an additional step in the data analysis and also allows an assessment of the enhanced FR concentration distribution in the close vicinity of the reinforcement. This sample vividly demonstrates the need for multienergy tomography as not all X-ray energies yield high-contrast images.

Experimental Section

Sample Preparation. A short-chain, partially brominated polystyrene flame retardant (Figure 1 with $x = 3$) and its

synergist, antimony(III) oxide, were blended in a twin-screw reactor at 285 °C with a dry mixture of nylon, Teflon, and fiberglass and extruded as a rod. The nylon and fiberglass were supplied as the composite material, Zytel-70G43L. From the formulation in the 1000 g batch preparation and the Br and Sb analyses, the sample composition (vol %) was FR, 10.86; Sb_2O_3 , 1.42; nylon, 63.84; SiO_2 , 23.56; and Teflon, 0.31. More details are given in Table S1 (Supporting Information). The vol % values were calculated from the component densities, assuming additive volumes.

Synchrotron X-ray Tomography. Tomography was done at the Advanced Photon Source (APS), Argonne National Laboratory, at bending magnet 13-BM-D in the GeoSoilEnviroCARS (GSECARS) group.³² The X-ray beam was defined with a double Si-111 crystal monochromator yielding X-rays in the range of 8 to 65 keV with a beam size up to 50 mm wide and 5 mm high at the sample rotation stage.³³ Transmitted X-rays were converted to light with a 500 μm thick Ce:YAG scintillator and imaged with a 10 \times Mitutoyo microscope objective focused onto a 12 bit CCD camera (Roper Scientific MicroMAX 5 MHz) with 1300 \times 1100 pixels (pixel size 7 μm); a combination of optical magnification and binning yields 3.26 $\mu\text{m} \times$ 3.26 μm resolution. The sample was turned into a cylinder with a diameter at midheight of approximately 1.52 mm and mounted with clay atop the tomography sample rotation stage. A total of 720 images were collected as the sample was rotated from 0 to 179.5° by a 0.5° step size and then from 0.25 to 179.75° by a 0.5° step size. Over the course of the imaging experiment, the X-ray flux at the sample was stabilized to within a few percent with two mechanisms. The APS beam current was held constant by operation in “top-up mode”. The orientation of the second crystal of the monochromator was fine-tuned based on feedback from an ion chamber X-ray flux indicator mounted immediately upstream of the sample. The sample was imaged at 12, 13.4, 17, 25, 30.43, 30.53, and 40 keV with an X-ray band-pass of $\Delta E/E = 10^{-4}$; the Br and Sb K-edges were at 13.47 and 30.49 keV, respectively.

Each CCD image was converted to an absorbance image with white field and average dark count correction. White field images were collected at intervals of 50 CCD images. The average dark field intensity was 100 counts. Sinograms were constructed; efforts were made to reduce zingers³⁴ and ring artifacts. The slice reconstruction was done with a fast Fourier transform algorithm following a regridding from polar to Cartesian coordinate systems.³³ The slices were assembled into a single reconstructed volume of 650 \times 650 \times 515 volume elements, each element containing a value of the voxel absorbance.

The 2D FFT-based reconstruction introduces scale ($\leq 6.5\%$), offset ($\leq 4 \times 10^{-4}$), and voxel size ($\leq 2.7\%$) errors in the voxel absorbances, and these were corrected by rescaling, eq 1, such that projections of representative slices yield absorbances in agreement with the original absorbance images. Note that when calculating projections from the 3D data sets, only the voxels within the reconstructed radon-defined circle were used; the absorbance values for positions lying between the inscribed circle and the square defined by data storage were not used as these areas are not defined by the radon transform. The correction factors were independently determined for each sample at each X-ray energy, as listed in Table S3 (Supporting Information).

$$A_{xyzE}^{\text{expt}} = [A_{xyzE}^{\text{raw}} \xrightarrow{\text{voxel size}} A_{xyzE}] \times \text{scale}_E + \text{offset}_E \quad (1)$$

3D compositions are calculated from the experimental voxel absorbance and the voxel linear attenuation coefficients for the pure components. The NIST XCOM database reports mass attenuation coefficients,³⁵ and these are converted to voxel linear attenuation coefficients for 3.26 μm voxels, as listed in Table 1. The voxel linear attenuation coefficients are equal to the mass attenuation coefficient (cm^2/g) \times density (g/cm^3) \times voxel dimension (cm).

From the corrected reconstructed volumes, a cuboid subvolume of $200 \times 200 \times 500$ voxels was selected for further analysis at the coordinate listed in Table S4 (Supporting Information). The subvolume was chosen to exclude air; however, a small internal air-filled crack was captured in the subvolume, and these air-filled voxels, 0.0703% of the subvolume, were excluded by a binary air mask from further calculation.

3D Composition Calculation. The 3D chemical concentration distributions of **FR**, Sb_2O_3 , and SiO_2 were calculated for all voxels in the subvolume (excluding the air crack voxels). A least-squares fit to the voxel linear attenuation coefficients of Table 1 was made based on a Beer's law absorbance model³⁶

$$A_{xyzE}^{\text{calc}} = [\text{FR}]_{xyz} \times A_E^{\text{FR}} + [\text{Sb}_2\text{O}_3]_{xyz} \times A_E^{\text{Sb}_2\text{O}_3} + [\text{SiO}_2]_{xyz} \times A_E^{\text{SiO}_2} + (1 - [\text{FR}]_{xyz} - [\text{Sb}_2\text{O}_3]_{xyz} - [\text{SiO}_2]_{xyz}) \times A_E^{\text{matrix}} \quad (2)$$

where A_E^{FR} is the absorbance of voxel completely filled with **FR** at energy E , as listed in Table 1; $A_E^{\text{Sb}_2\text{O}_3}$ and $A_E^{\text{SiO}_2}$ are similarly defined. The X-ray absorbance for the nylon/Teflon blend, A_E^{matrix} , is defined as a weighted average

$$A_E^{\text{matrix}} = \frac{[\text{nylon}] \times A_E^{\text{nylon}} + [\text{Teflon}] \times A_E^{\text{Teflon}}}{[\text{nylon}] + [\text{Teflon}]} \quad (3)$$

where A_E^{nylon} and A_E^{Teflon} are the absorbances of voxels completely filled with nylon or Teflon, respectively, at energy E , as listed in Table 1.

The parenthetical term in eq 2 restricts application of the model to voxels completely filled with sample, that is, no cracks, voids, or surface voxels. The concentrations are determined with a minimization of difference between the experimental X-ray voxel absorbances and the calculated absorbances. The fit parameters, $[\text{FR}]_{xyz}$, $[\text{Sb}_2\text{O}_3]_{xyz}$, and $[\text{SiO}_2]_{xyz}$, are constrained to have physically reasonable values between 0 and 100 vol %, inclusive. These 3D chemical compositions of $[\text{FR}]_{xyz}$, $[\text{Sb}_2\text{O}_3]_{xyz}$, and $[\text{SiO}_2]_{xyz}$ of a $200 \times 200 \times 500$ cuboid are then used to analyze the radial concentration distribution about the fiberglass bundles.

TABLE 1: Calculated Voxel Linear Attenuation Coefficients of Pure Components for 3.26 μm Voxels

energy/keV	nylon	SiO_2	FR	Sb_2O_3	Teflon
12	0.000645	0.00795	0.0153	0.139	0.00285
13.4	0.000480	0.00578	0.0113	0.104	0.00207
17	0.000270	0.00289	0.0409	0.0545	0.00106
25	0.000135	0.000996	0.0146	0.0194	0.000412
30.43	0.000107	0.000604	0.00853	0.0115	0.000282
30.53	0.000107	0.000600	0.00845	0.0629	0.000280
40	0.0000866	0.000333	0.00403	0.0314	0.000190

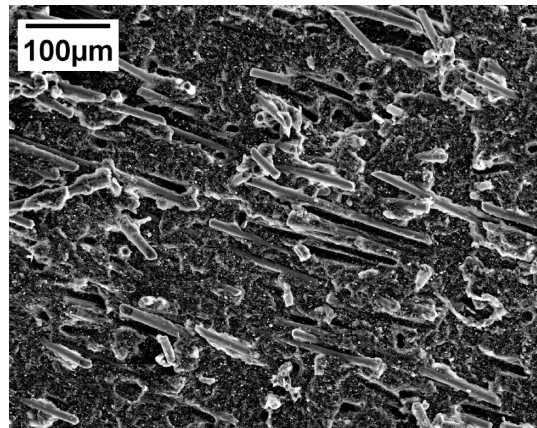


Figure 3. SEM image of the freeze-fractured sample showing the embedded fiberglass in a nylon matrix. Each glass fiber is $\sim 10 \mu\text{m}$ in diameter³⁷ and $\sim 100 \mu\text{m}$ in length.

Scanning Electron Microscopy. The sample was freeze-fractured in liquid N_2 and then coated with a 10 nm thick carbon layer for microscopy with a JEOL-840 SEM. The secondary electron image, Figure 3, was acquired at 20 kV.

Results and Discussion

X-ray Absorbance and Tomographic Reconstructions. The absorbance images of the sample at two representative X-ray energies below and above the Br K-edge, 12 and 25 keV, respectively, are shown in Figure 4. The light-colored striations observed at 12 keV are due to bundles of glass fibers; at this energy, SiO_2 has greater attenuation, 0.00795, than any other component, including the well-mixed **FR** in nylon. The bundle sizes are much larger than an individual fiber, probably consisting of 10–30 fibers. Interestingly, the bundles disappear at 25 keV, and this will be attributed to accumulation of **FR** near the SiO_2 fibers, giving each bundle the same X-ray attenuation as **FR**/nylon. As noted in Figures 4a and 5, the fiberglass bundles are roughly aligned along the tomography Z-axis, which also corresponds to the extrusion axis of the cylindrical sample.

3D Binary Mask of SiO_2 -Rich Voxels. On the basis of the sample formulation, some voxels will be completely filled with SiO_2 , while other voxels may contain a **FR**/ Sb_2O_3 /nylon blend. To aid the analysis, a 3D binary mask is defined based on the voxels with high SiO_2 concentrations, as calculated in a later section. The 3D binary fiberglass mask is based on an isosurface, with island removal, using a threshold of $[\text{SiO}_2] = 45 \text{ vol } \%$, yielding a mask with 2.58% voxels identified as SiO_2 -rich. (We also tested a binary mask derived from the intersection of high-absorbance voxels in the 12 and 13.4 keV subvolumes and found nearly equivalent results for fiber identification and bulk concentrations of the components.) The mask, Figure 5, shows fiberglass bundles and line segments representing the principal axes of 10 selected fiber bundles. Line probes show that most bundles have a radius on the order of 10–15 μm . Ten bundles were selected for further analysis; bundle coordinates are given in Table S5 (Supporting Information). Figure 5 illustrates the dense bundles conceptualized in Figure 2, but we should also recall the widespread distribution of fibers as shown in the SEM image of Figure 3.

Voxel Absorbance Values. The motivating question in this 3D chemical analysis is the distribution of the **FR** and Sb_2O_3 synergist within the polymer blend and in the vicinity of the fiberglass bundles. A preliminary blending assessment can be

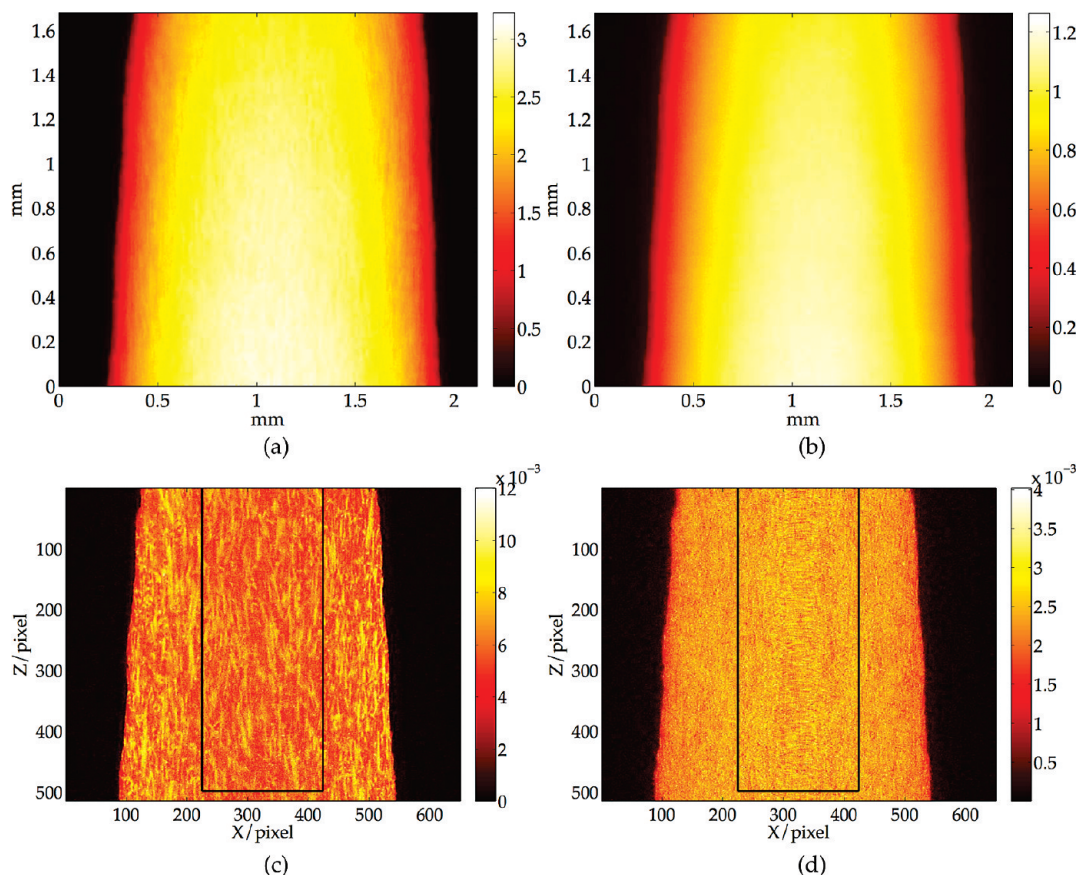


Figure 4. A comparison of 2D absorbance images, (a) 12 and (b) 25 keV, with XZ-slices from 3D reconstructions, (c) 12 and (d) 25 keV, respectively. The color bars for the 2D images (a,b) are total absorbance in the sample, while the color bars for the slices (c,d) describe absorbance in the $3.26\ \mu\text{m}$ voxels. The black rectangle (c,d) outlines the cuboid subvolume chosen for analysis. The light striations (a,c) are the fiberglass bundles which have, at 12 keV, more X-ray absorbance than the **FR**/nylon blend.

obtained from an analysis of the average voxel absorbance as a function of X-ray energy, as shown in Figure 6. The average values are shown pairwise, polymer-rich voxels with filled symbols and SiO_2 -rich with empty symbols, where voxel identification is based on the binary fiberglass mask (Figure 5).

The average voxel absorbance shows the expected increases at Br and Sb K-edges. An interesting feature is the contrast change between SiO_2 -rich and polymer-rich voxels. At X-ray energies below the Br K-edge, SiO_2 -rich voxels are more absorbing, as noted in Figures 4a,c and 6. Above the Br K-edge, both SiO_2 -rich and polymer-rich voxels have the same average X-ray absorbance, as shown in Figures 4b,d and 6. Later, this imaging problem will be attributed to enhanced **FR** and Sb_2O_3 concentrations near the fiberglass bundles (see Figure 12).

To assess the signal-to-noise of the reconstructed volumes, a histogram of the absorbance values of air-filled voxels is plotted in Figure 7. These voxels are defined by a $40 \times 200 \times 300$ cuboid outside of the sample but contained within the radius of reconstructed data, that is, the poorly defined voxels at the corners of the slices were excluded. In the noise-free limit, all histograms of air-filled voxels would be delta functions centered at zero absorbance. Here, at X-ray energies at which the sample has the greatest average absorbance, the X-ray flux at the scintillator is smallest, causing a greater contribution from shot noise.³⁶

The absorbance histograms, Figure 8, of the polymer-rich voxels, chosen with the aid of the binary fiberglass mask, show the expected decrease in absorbance with increasing X-ray energy. The mean voxel absorbances at each X-ray energy are plotted in Figure 6 as filled symbols and compared with the

voxel linear attenuation coefficients for voxels fully occupied by **FR**, Sb_2O_3 , or nylon. The widths of each mode are about twice that measured for air-filled voxels, Figure 7. In summary, the single, relatively narrow mode at all X-ray energies, as well as the mean absorbance values, indicates good blending of both **FR** and Sb_2O_3 in nylon.

3D Chemical Composition. The calculated vol % concentrations of **FR**, Sb_2O_3 , and SiO_2 were obtained from the multi-energy X-ray tomography data and the three-parameter model, eq 2, for almost all of the cuboid's 2×10^7 voxels, except the 0.07% of cuboid voxels identified as an internal air-filled crack. The calculated SiO_2 vol % concentration cuboid was converted into a binary fiberglass mask using a threshold value of $[\text{SiO}_2] = 45\ \text{vol \%}$, as shown in Figure 5; 2.58% of the cuboid voxels were thus identified as predominantly SiO_2 . The binary fiberglass mask is very conservative, as the sample formulation shows a fiberglass concentration of 23.56 vol %; the difference between the formulation and the binary mask is due to the small size of the glass fibers, about $10 \times 100\ \mu\text{m}$, relative to the voxel size of $3.26\ \mu\text{m}$, creating many voxels only partially occupied by SiO_2 .

The calculated vol % concentrations of **FR** and Sb_2O_3 are shown as histograms in Figure 9. The mean **FR** concentration in the polymer-rich voxels is 10.41 vol % ($\sigma = 1.9\ \text{vol \%}$) compared with chemical analysis of 10.86 vol % for the entire sample. Similarly, tomography shows $[\text{Sb}_2\text{O}_3] = 1.73\ \text{vol \%}$ ($\sigma = 0.56\ \text{vol \%}$), while chemical analysis gives 1.42 vol %. Contributions to the standard deviation come from shot noise in the tomography experiment,³⁶ from voxel-to-voxel fluctuations in the chemical concentration,¹⁰ and from the voxels

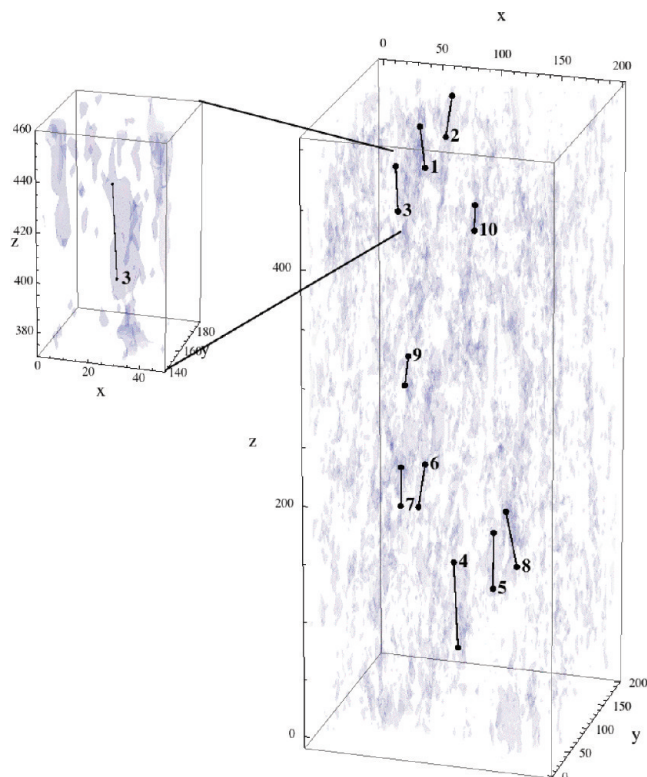


Figure 5. A $200 \times 200 \times 500$ cuboid binary mask for fiberglass based on the reconstructed volume for SiO_2 . This mask is conservative with 2.58% of the cuboid voxels selected, compared to the 23.56 vol % of fiberglass in the sample based on formulation. Also shown are line segments representing the principal axes of 10 selected fiber bundles.

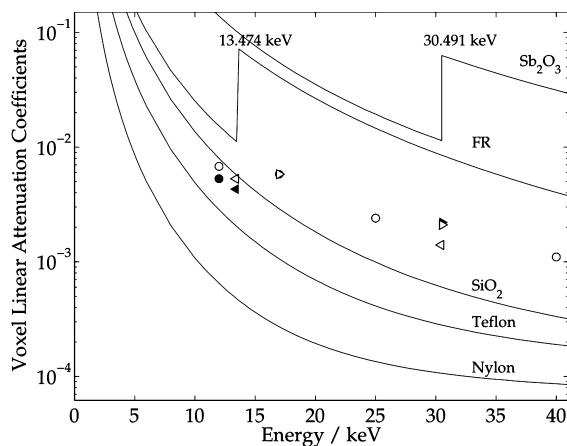


Figure 6. The traces show the calculated voxel linear attenuation coefficients for the pure components (see Table 1). The average voxel absorbance values for the two sets of voxels identified by the binary fiberglass mask; the polymer-rich voxels are represented by filled (●, left-pointing triangle, right-pointing triangle) symbols and the average values for the SiO_2 -rich voxels by open (○, left-pointing triangle, right-pointing triangle) symbols, which at some X-ray energies overlap the filled symbols.

partially or fully occupied by glass fibers, yet not removed from analysis by the binary fiberglass mask.

A 3D view of a well-blended mixture should look rather bland and without structure, as seen for both **FR** and Sb_2O_3 in Figure 10. Here, the binary fiberglass mask has not been applied, and all calculated voxel concentrations are shown. The dark structures in **FR** are due to the fiberglass bundles. More importantly, the **FR** is well-blended throughout the sample, with

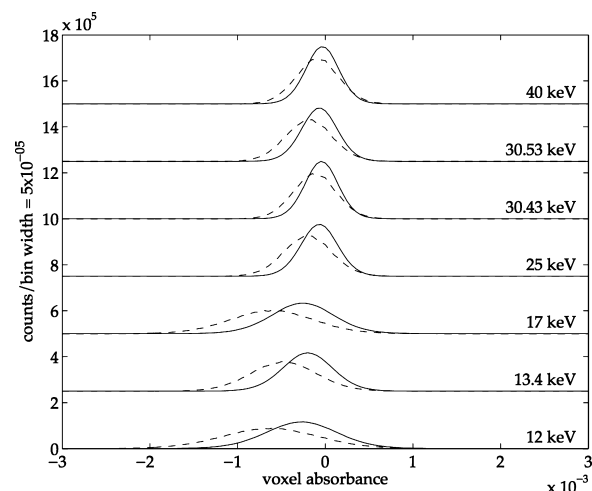


Figure 7. Histogram of air-filled voxels (traces shifted by 2.5×10^5). The standard deviation is determined by photon counting statistics and noise introduced by the back projection reconstruction. Dashed lines show apparent absorbance prior to scale and offset corrections, eq 1.

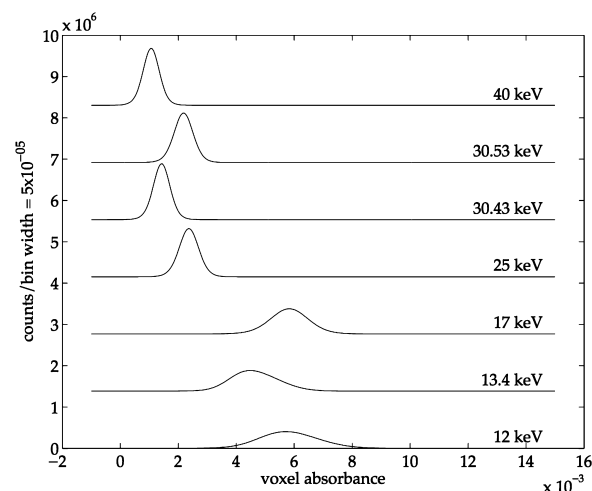


Figure 8. Voxel absorbances in the sample-filled $200 \times 200 \times 500$ cuboid for the polymer-rich voxels, selected based on the binary fiberglass mask, Figure 5 (traces shifted by 1.39×10^6). Overall, the sample becomes more transparent at higher X-ray energies but with the Br and Sb K-edge absorbances evident at 17 and 30.53 keV, respectively.

no indication of regions of excessively high or low **FR** concentrations, and it is similar for Sb_2O_3 . A 3D view of the SiO_2 concentration is shown in Figure 5 as an isosurface at $[\text{SiO}_2] = 45$ vol %.

Radial Concentration about Fiber Bundles. Figure 2 shows a simplistic model for **FR** concentrations near the fiberglass bundles. More sophisticated models such as the Flory–Huggins theory for polymer blends note the importance of component interaction enthalpies.³⁸ In Figure 2, we assume no special affinity or aversion of **FR** with SiO_2 but simply $\chi_{\text{FR}/\text{SiO}_2} = \chi_{\text{FR}/\text{nylon}}$, and similarly for Sb_2O_3 , where χ is the enthalpy term. Yet, the curious change in image structure with increasing X-ray energy (see Figure 4c,d and also note the equivalence in mean voxel absorbance for SiO_2 -rich and polymer-rich voxels in Figure 6) suggest an enhanced concentration of **FR** and Sb_2O_3 within the fiberglass bundles, which implies an enthalpy-driven concentration gradient. How might we use the tomography results to assess the **FR** concentration in the vicinity of the fiberglass bundles?

Starting with the binary fiberglass mask, Figure 5, we identified 10 well-formed bundles, all relatively isolated. Each

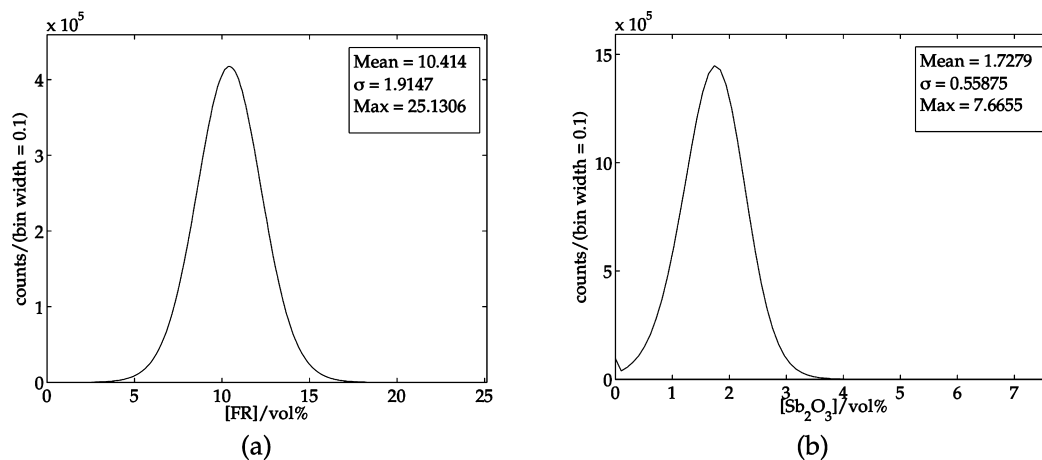


Figure 9. Concentrations of (a) **FR** and (b) Sb_2O_3 in the $3.26\ \mu\text{m}$ voxels in the cuboid. The mean values agree with sample formulation, and the relatively small standard deviations indicate good blending with nylon.

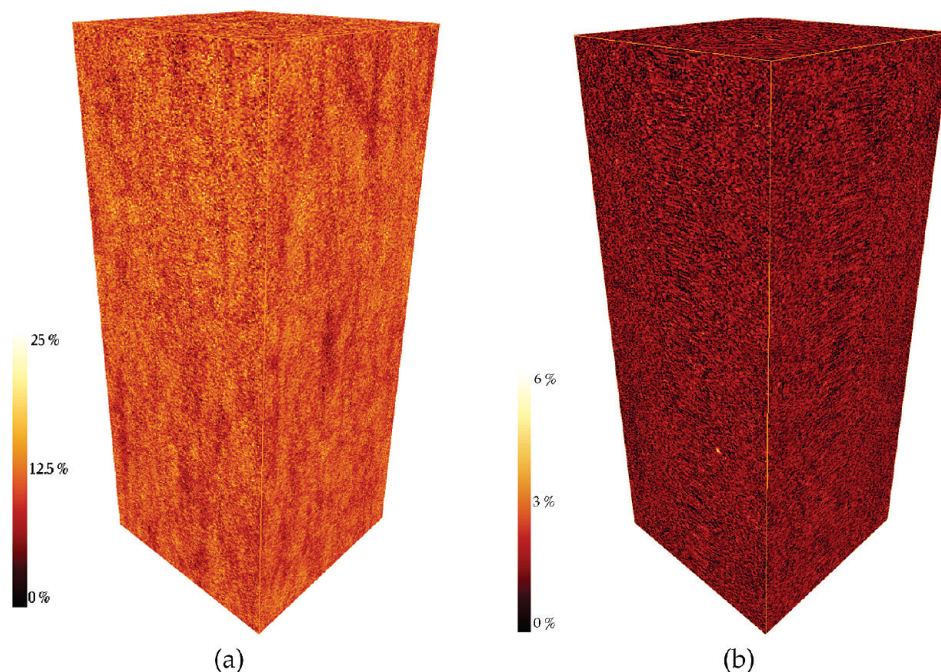


Figure 10. 3D renderings of the concentrations for (a) **FR** and (b) Sb_2O_3 for the $200 \times 200 \times 500$ cuboid subvolume with $3.26\ \mu\text{m}$ voxels. The color bars indicate concentrations in vol %.

bundle is cylindrical, roughly $20\ \mu\text{m}$ in radius. The line segments defining the cylinder axis are listed in Table S5 (Supporting Information). All voxels surrounding the cylinder axes up to a radius of $50\ \mu\text{m}$ (15 voxels) were located and assessed for collision with neighboring glass fibers, again using the binary fiberglass mask. A collision will remove a voxel from further consideration, as well as other voxels along that same radial vector away from the cylinder axis. The voxels retained were sorted by Euclidean distance from a cylinder axis, and the corresponding voxel concentrations were used to generate the radial concentration plots shown in Figure 11. The voxel selection procedure is described in the Supporting Information. A simple histogram of the number of voxels contributing to a radial concentration plot about a cylindrical axis will show a linear increase in voxel count, as shown in the upper trace of Figure 11b; the bar graph shows the voxels actually used in the concentration analysis for the 10 selected fiber bundles out to a search radius of $50\ \mu\text{m}$.

The SiO_2 radial concentration, Figure 11a, is averaged over the 10 fiber bundles and shows several features: (1) The average

fiber bundle radius is about $20\ \mu\text{m}$, in agreement with Figures 4b and 5. (2) The fibers are loosely arranged into bundles as the maximum SiO_2 concentration is 52.8 vol %, indicating significant polymer flow into the fiber bundles, consistent with the SEM imaging, Figure 3. (3) At $r = 50\ \mu\text{m}$, the SiO_2 concentration drops to about 20 vol %, close to the sample formulation value of 23.31 vol %. The SiO_2 radial concentration is fitted to a Gaussian, $[\text{SiO}_2]_r = ae^{-(r/b)^2} + c$, and the coefficients are listed in Table S6 (Supporting Information); the value of b is $19.5 \pm 0.5\ \mu\text{m}$. The dashed traces in Figure 11c,d are drawn based on the changing SiO_2 concentration and the bulk concentrations of **FR** and Sb_2O_3 : $[\text{FR}]_r^{r=0} = c_{\text{FR}} \times [1 - a_{\text{SiO}_2}e^{-(r/b_{\text{SiO}_2})^2}]$ and $[\text{Sb}_2\text{O}_3]_r^{r=0} = c_{\text{Sb}_2\text{O}_3} \times [1 - a_{\text{SiO}_2}e^{-(r/b_{\text{SiO}_2})^2}]$.

The radial concentrations of **FR** and Sb_2O_3 in the vicinity of the 10 selected fiber bundles are plotted in Figure 11c,d, respectively. As expected, the concentrations decrease at small r , when voxels lying within a fiber bundle are inspected for **FR** and Sb_2O_3 concentrations; many of these voxels are partially occupied with SiO_2 . However, the decrease in **FR** and Sb_2O_3 concentrations is not as dramatic as predicted based upon the

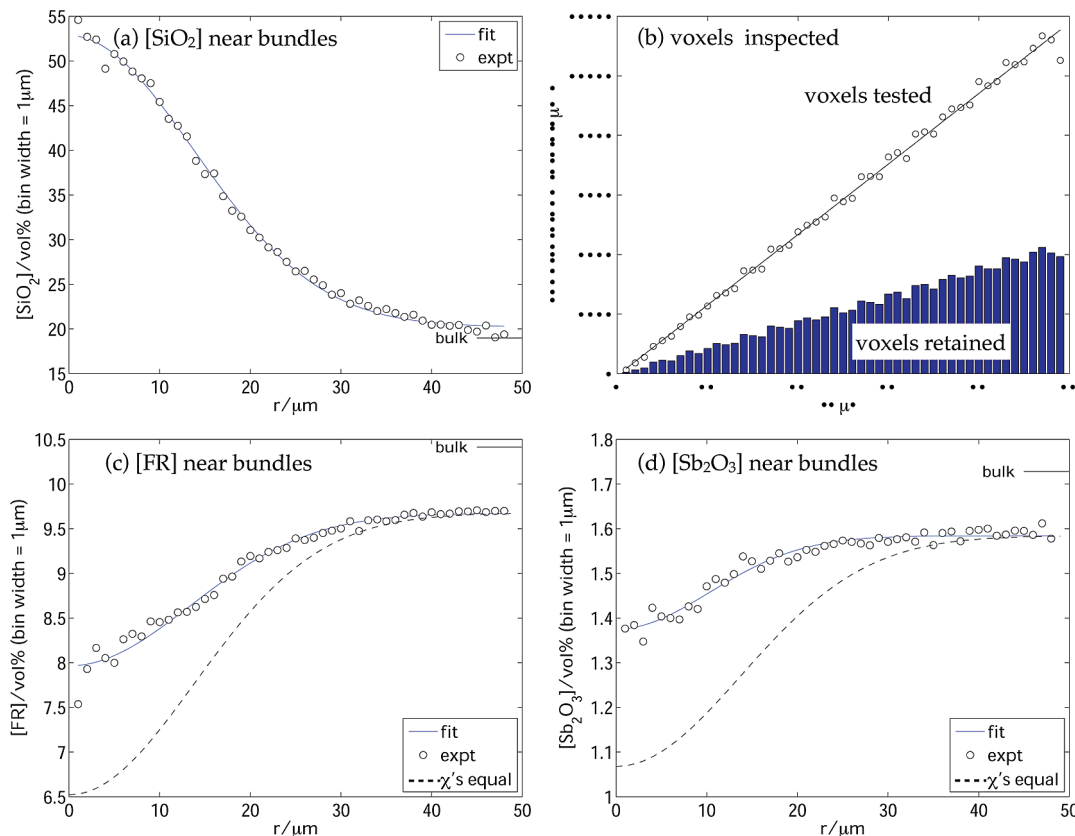


Figure 11. The radial concentration of (a) SiO_2 as a function of distance from the fiber bundle axes, sampled over 10 fiber bundles. Collision detection reduces the number of sampled voxels (b) at large r . The radial concentrations for (c) **FR** and (d) Sb_2O_3 and comparisons with a space-filling model based on the radial concentration of SiO_2 . The “bulk” concentrations are the average values for those 97.42% of the voxels not identified as SiO_2 -rich in Figure 5: $[\text{SiO}_2]_{\text{bulk}} = 19.00$ vol %, $[\text{FR}]_{\text{bulk}} = 10.41$ vol %, $[\text{Sb}_2\text{O}_3]_{\text{bulk}} = 1.73$ vol % (Figure 9a), and $[\text{Sb}_2\text{O}_3]_{\text{bulk}} = 1.73$ vol % (Figure 9b).

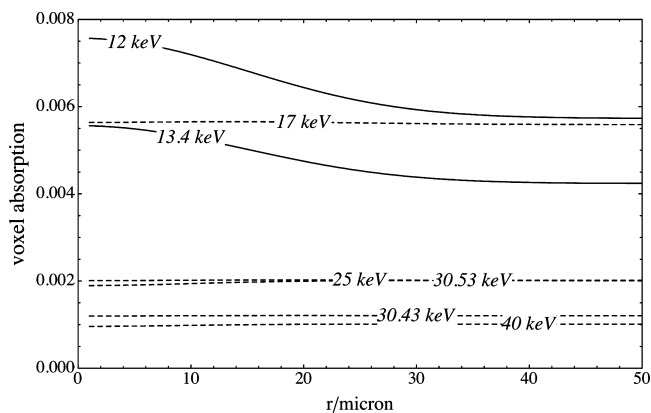


Figure 12. Why are the SiO_2 fiber bundles visible at 12 keV and invisible at 25 keV? The change in X-ray voxel absorbance is calculated based on the radial concentrations (Figure 11 (fits)) and the pure-phase voxel linear attenuation coefficients (Table 1). All traces move up and down, as experimentally found with the average experimental voxel absorbance values given in Figure 6, with $r = 0 \mu\text{m}$ corresponding to the open symbols and $r = 50 \mu\text{m}$ corresponding to the filled symbols.

volume of SiO_2 present. Shown in both panels are predicted concentrations assuming that a simple space-filling model applies, for example, Figure 2. For both **FR** and Sb_2O_3 , the concentrations are 30% greater within the fiber bundles, relative to the space-filling model. One possible explanation is that the hydrophobic coatings applied to the glass fibers leads to precipitation of **FR** and Sb_2O_3 onto the fibers.

Image Contrast with X-ray Energy. Now that $[\text{FR}]_r$ and $[\text{Sb}_2\text{O}_3]_r$ are known, we can consider the cause of the poor image

contrast shown in Figure 4d taken at 25 keV versus the excellent image contrast in Figure 4c at 12 keV. We can use the radial concentrations to calculate the voxel absorbance both as a function of X-ray energy and as a function of radial distance from the center of the fiber bundles, as shown in Figure 12. The traces at 12 and 13.4 keV show that high concentrations of SiO_2 are more X-ray-absorbing than the rest of the sample and are thus visible as white streaks at 12 keV in Figure 4c. However, at 17 keV and above, X-ray absorbance changes due to decreasing SiO_2 with r are balanced by increasing X-ray absorbance as **FR** and Sb_2O_3 concentrations increase, yielding a constant voxel absorbance as a function of radial distance from the fiber bundles. This constant X-ray absorbance then yields the curiously low contrast image at 25 keV, Figure 4d.

Conclusion

Three-dimensional chemical analysis is shown here as an effective method for studying a polymer blend, even with a composite material reinforcement. An analysis procedure was developed to generate radial concentrations measurements about cylindrical composites, measurements which reveal unique information about the polymer blend structure.

Acknowledgment. The authors gratefully acknowledge financial support from the National Science Foundation, CHE-0517326. The tomography beamline at CAMD acknowledges the support of the NSF IMR-0216875 (monochromator) and the State of Louisiana through the CAMD operational budget. Use of the Advanced Photon Source was supported by the U.S. Department of Energy, Basic Energy Sciences, Office of Science, under Contract No. W-31-109-Eng-38. Use of the

scanning electron microscope was provided by Dr. Xiaogang Xie of the Department of Geology and Geophysics, LSU, Baton Rouge, LA. We thank Dr. Larry Simeral of Albermarle Corporation for his advice with this project.

Supporting Information Available: A table of pure component densities; Matlab code fragment for applying scale, offset, and voxel size corrections to the reconstructed APS tomography volumes; table of scale, offset, and voxel size correction factors; table of subvolume origin within the APS tomography volume; table of fiber coordinates; and notes for the derivation of the radial concentration algorithm. This material is available free of charge via the Internet at <http://pubs.acs.org>. This material is available free of charge via the Internet at <http://pubs.acs.org>.

References and Notes

- (1) Natterer, F.; Ritman, E. L. Past and future directions in X-ray computed tomography (CT). *Int. J. Imaging Systems Technol.* **2002**, *12*, 175–187.
- (2) Herman, G. T.; Kuba, A. Eds.; *Discrete Tomography*; Birkhäuser: Boston, MA, 1999.
- (3) Epstein, C. L. *Mathematics of Medical Imaging*; Prentice Hall: New York, 2003.
- (4) Lohmann, G. *Volumetric Image Analysis*; Wiley-Teubner: New York, 1998.
- (5) Sapiro, G. *Geometric Partial Differential Equations and Image Analysis*; Cambridge University Press: New York, 2001.
- (6) Spanne, P.; Thovet, J. F.; Jacquin, C. J.; Lindquist, W. B.; Jones, K. W.; Adler, P. M. Synchrotron computed microtomography of porous media: topology and transports. *Phys. Rev. Lett.* **1994**, *73*, 2001–4.
- (7) Lindquist, W. B.; Lee, S.-M.; Coker, D. A.; Jones, K. W.; Spanne, P. Medial Axis Analysis of Void Structure in Three Dimensional Tomographic Images of Porous Media. *J. Geophys. Res. B* **1996**, *101*, 8297–8310.
- (8) Butler, L. G.; Owens, J. W.; Cartledge, F. K.; Kurtz, R. L.; Byerly, G. R.; Wales, A. J.; Bryant, P. L.; Emery, E. F.; Dowd, B.; Xie, X. G. Synchrotron X-ray microtomography, electron probe microanalysis, and NMR of toluene waste in cement. *Environ. Sci. Technol.* **2000**, *34*, 3269–3275.
- (9) Schroer, C. G.; Cloetens, P.; Rivers, M.; Snigirev, A.; Takeuchi, A.; Yun, W. B. High-resolution 3D imaging microscopy using hard X-rays. *MRS Bull.* **2004**, *29* (3), 157–165.
- (10) Ham, K.; Jin, H.; Al-Raoush, R. I.; Xie, X. G.; Willson, C. S.; Byerly, Larry, G. R.; Simeral, S.; Rivers, M. L.; Kurtz, R. L.; Butler, L. G. Three-Dimensional Chemical Analysis with Synchrotron Tomography at Multiple X-ray Energies: Brominated Aromatic Flame Retardant and Antimony Oxide in Polystyrene. *Chem. Mater.* **2004**, *16*, 4032–4042.
- (11) Le Gros, M. A.; McDermott, G.; Larabell, C. A. X-ray tomography of whole cells. *Curr. Opin. Struct. Biol.* **2005**, *15*, 593–600.
- (12) Marschallinger, R. Three-dimensional reconstruction and modeling of microstructures and microchemistry in geological materials. *Scanning* **1998**, *20*, 65–73.
- (13) Muller-Reichert, T.; Hohenberg, H.; O'Toole, E. T.; McDonald, K. Cryoimmobilization and three-dimensional visualization of *C-elegans* ultrastructure. *J. Microsc. (Oxford, U.K.)* **2003**, *212*, 71–80.
- (14) Pittsburgh Supercomputer Center. The Visible Human Project at the National Library of Medicine; http://www.nlm.nih.gov/research/visible/visible_human.html (accessed August, 2008).
- (15) Heldele, R.; Rath, S.; Merz, L.; Butzbach, R.; Hagelstein, M.; Hausselt, J. X-ray tomography of powder injection moulded micro parts using synchrotron radiation. *Nucl. Instrum. Methods Phys. Res., Sect. B* **2006**, *246*, 211–216.
- (16) Schilling, P. J.; Karedla, B. P. R.; Tatiparthi, A. K.; Verges, M. A.; Herrington, P. D. X-ray computed microtomography of internal damage in fiber reinforced polymer matrix composites. *Compos. Sci. Technol.* **2005**, *65*, 2071–2078.
- (17) Momose, A.; Fujii, A.; Kadowaki, H.; Jinnai, H. Three-dimensional observation of polymer blend by X-ray phase tomography. *Macromolecules* **2005**, *38*, 7197–7200.
- (18) Maire, E.; Gimenez, N.; Sauvante-Moynot, V.; Sautereau, H. X-ray tomography and three-dimensional image analysis of epoxy–glass syntactic foams. *Philos. Trans. R. Soc. London, Ser. A* **2006**, *364*, 69–88.
- (19) Alderden, R. A.; Mellor, H. R.; Modok, S.; Hall, M. D.; Sutton, S. R.; Newville, M. G.; Callaghan, R.; Hambley, T. W. Elemental tomography of cancer-cell spheroids reveals incomplete uptake of both platinum(II) and platinum(IV) complexes. *J. Am. Chem. Soc.* **2007**, *129*, 13400–13401.
- (20) Gass, M. H.; Koziol, K. K. K.; Windle, A. H.; Midgley, P. A. Four-dimensional spectral tomography of carbonaceous nanocomposites. *Nano Lett.* **2006**, *6*, 376–379.
- (21) Friedrich, H.; Sietsma, J. R. A.; de Jongh, P. E.; Verkleij, A. J.; de Jong, K. P. Measuring location, size, distribution, and loading of NiO crystallites in individual SBA-15 pores by electron tomography. *J. Am. Chem. Soc.* **2007**, *129*, 10249–10254.
- (22) Elmoutaouakkil, A.; Fuchs, G.; Bergounhon, P.; Péres, R.; Peyrin, F. Three-dimensional quantitative analysis of polymer foams from synchrotron radiation X-ray microtomography. *J. Phys. D: Appl. Phys.* **2003**, *36*, A37–43.
- (23) Yoon, J. H.; Kawamura, T.; Takeya, S.; Jin, S. K.; Yamamoto, Y.; Komai, T.; Takahashi, M.; Nawaby, A. V.; Handa, Y. P. Probing Fickian and non-Fickian diffusion of CO₂ in poly(methyl methacrylate) using in situ Raman spectroscopy and microfocus X-ray computed tomography. *Macromolecules* **2004**, *37*, 9302–9304.
- (24) Yamauchi, K.; Takahashi, K.; Hasegawa, H.; Iatrou, H.; Hadjichristidis, N.; Kaneko, T.; Nishikawa, Y.; Jinnai, H.; Matsui, T.; Nishioka, H.; Shimizu, M.; Fukukawa, H. Microdomain morphology in an ABC 3-miktoarm star terpolymer: A study by energy-filtering TEM and 3D electron tomography. *Macromolecules* **2003**, *36*, 6962–6966.
- (25) Takano, A.; Wada, S.; Sato, S.; Araki, T.; Hirahara, K.; Kazama, T.; Kawahara, S.; Isono, Y.; Ohno, A.; Tanaka, N.; Matsushita, Y. Observation of cylinder-based microphase-separated structures from ABC star-shaped terpolymers investigated by electron computerized tomography. *Macromolecules* **2004**, *37*, 9941–9946.
- (26) Barnett, H. A.; Ham, K.; Butler, L. G. Synchrotron X-ray tomography for 3D chemical diffusion measurement of a flame retardant in polystyrene. *Nucl. Instrum. Methods Phys. Res., Sect. A* **2007**, *582*, 202–204.
- (27) Ham, K.; Barnett, H. A.; Butler, L. G. Burning issues in tomography analysis. *Comput. Sci. Eng.* **2008**, *10*, 78–81.
- (28) Simonson, M. Effect of FR enclosures on the fire behavior of TV sets. *Polym. Mater. Sci. Eng.* **2000**, *83*, 90–91.
- (29) De Schryver, D.; Landry, S. D.; Reed, J. S. Latest developments on the flame retardancy of engineering thermoplastics - SAYTEX HP-7010 (brominated polystyrene) in glass filled engineering thermoplastics. *Polym. Degrad. Stab.* **1999**, *64*, 471–477.
- (30) Litzemberger, A. Criteria for, and examples of optimal choice of flame retardants. *Polym. Polym. Compos.* **2000**, *8*, 581–592.
- (31) Randoux, T.; Vanovervelt, J. C.; Van den Bergen, H.; Camino, G. Halogen-free flame retardant radiation curable coatings. *Prog. Org. Coat.* **2002**, *45*, 281–289.
- (32) Spanne, P.; Rivers, M. L. Computerized microtomography using synchrotron radiation from the NSLS. *Nucl. Instrum. Methods Phys. Res., Sect. B* **1987**, *24–25*, 1063–7.
- (33) Rivers, M. L. Tutorial introduction to X-ray computed microtomography; <http://www-fp.mcs.anl.gov/xray-cmt/rivers/tutorial.html> (accessed August, 2008).
- (34) Gruner, S. M.; Tate, M. W.; Eikenberry, E. F. Charge-coupled device area X-ray detectors. *Rev. Sci. Instrum.* **2002**, *73*, 2815–2842.
- (35) NIST XCOM: Photon Cross Sections Database; <http://physics.nist.gov/PhysRefData/Xcom/Text/XCOM.html> (accessed August 2008).
- (36) Ham, K.; Butler, L. G. Algorithms for three-dimensional chemical analysis via multienergy synchrotron X-ray tomography. *Nucl. Instrum. Methods Phys. Res., Sect. B* **2007**, *262*, 117–127.
- (37) Davis, J. A.; Laskowski, T. T. Materials analysis of fiberglass-reinforced plastics by scanning electron microscopy. *Microbeam Anal.* **1985**, *7*, 193–196.
- (38) Hsu and, C. C.; Prausnit, J. M. Thermodynamics of polymer compatibility in ternary systems. *Macromolecules* **1974**, *7*, 320–324.